The Cryosphere Discuss., 8, 1589–1629, 2014
www.the-cryosphere-discuss.net/8/1589/2014/
doi:10.5194/tcd-8-1589-2014

The Cryosphere Discussions
Open Access

Representing moisture fluxes and phase changes in glacier debris cover using a single-reservoir approach

E. Collier[1,4], L. I. Nicholson[2], B. W. Brock[3], F. Maussion[4], R. Essery[5], and A. B. G. Bush[1]

[1]Department of Earth & Atmospheric Sciences, University of Alberta, Edmonton, Canada
[2]Institute of Meteorology and Geophysics, University of Innsbruck, Innsbruck, Austria
[3]Geography Department, Northumbria University, Newcastle upon Tyne, UK
[4]Chair of Climatology, Technische Universität Berlin, Berlin, Germany
[5]School of Geosciences, University of Edinburgh, Edinburgh, Scotland

Received: 27 February 2014 – Accepted: 11 March 2014 – Published: 19 March 2014

Correspondence to: E. Collier (eec@ualberta.ca)

Published by Copernicus Publications on behalf of the European Geosciences Union.

Abstract

Due to the complexity of treating moisture in supraglacial debris, surface energy balance models to date have neglected moisture infiltration and phase changes in the debris layer. The latent heat flux (QL) is also often excluded due to the uncertainty in determining the surface vapour pressure. To quantify the importance of moisture on the surface energy and climatic mass balance (CMB) of debris-covered glaciers, we developed a simple, single-reservoir parameterization for the debris ice and water content, as well as an estimation of the latent heat flux. The parameterization was incorporated into a sophisticated CMB model adapted for debris-covered glaciers. We perform two point simulations using both our new "moist" and the conventional "dry" approaches, on the Miage Glacier, Italy, during summer 2008 and fall 2011. The former simulation coincides with available in situ glaciological and meteorological measurements, including the first eddy-covariance measurements of the turbulent fluxes over supraglacial debris, while the latter contains two refreeze events that permit evaluation of the influence of phase changes. The simulations demonstrate a clear influence of moisture on the glacier energy and mass dynamics. Heat transmission to the underlying ice is lower, as the effective thermal diffusivity of the debris is reduced by increases in the weighted density and specific heat capacity when water and ice are considered. In combination with surface heat extraction by QL, sub-debris ice melt is reduced by 2.3 % in 2008 and by 2.8 % in 2011 when moisture effects are included. However, mass loss due to surface vapour fluxes more than compensates for the reduction in ice melt, such that the total accumulated ablation increased by 5.3 % in 2008 and by 2.8 % in 2011. Although the parameterization is a simplified representation of the moist physics of glacier debris, it is a novel attempt at including moisture in a numerical model of debris-covered glaciers and opens up additional avenues of future research.

TCD
8, 1589–1629, 2014

1 Introduction

Numerical modelling of debris-covered glaciers has received renewed scientific interest in recent years, as their contribution to changes in ice mass and water resources in many regions remains poorly understood (e.g. Kääb et al., 2012) and due to the fact that the proportion of debris-covered glacier is rising as glaciers recede (e.g. Stokes et al., 2007; Bolch et al., 2008; Bhambri et al., 2011).

It is well established that supraglacial debris exerts an important control on glacier melt rates. Sub-debris ice-melt rates are strongly enhanced when the debris thickness is less than a few centimeters, due to a reduction in surface albedo, an increase in absorption of shortwave radiation, and the rapid transfer of the energy to the underlying ice. Mass loss decreases exponentially as the thickness increases, as a result of insulation of the underlying glacier ice from the overlying atmosphere (e.g. Østrem, 1959; Loomis, 1970; Fujii, 1977; Inoue and Yoshida, 1980; Mattson et al., 1993). The presence of debris also alters the glacier surface energy balance, by permitting surface temperatures to rise above the melting point and by altering surface heat and moisture exchanges with the atmosphere (e.g. Brock et al., 2010).

Numerous point models of the surface energy of debris-covered glaciers have been developed to simulate sub-debris ice melt (e.g. Kraus, 1975; Nakawo and Young, 1982; Han et al., 2006; Nicholson and Benn, 2006; Reid and Brock, 2010). In recent years, models of debris cover have been extended to distributed simulations (Zhang et al., 2011). and to include both explicit calculation of heat conduction through a debris layer resolved into multiple levels and snow accumulation on top of the debris (Reid et al., 2012; Lejeune et al., 2013; Fyffe et al., 2014).

However, due to the complexity of treating moisture in supraglacial debris cover, surface energy balance models to date have neglected the latent heat and surface moisture flux components, with the exception of (1) testing the two end-member cases of completely dry or completely saturated debris layers (e.g. Nakawo and Young, 1981; Kayastha et al., 2000; Nicholson and Benn, 2006), and (2) using measurements of

TCD
8, 1589–1629, 2014

surface relative humidity to calculate the flux when the surface is saturated (Reid and Brock, 2010; Reid et al., 2012). In addition, moisture inputs to the debris layer – by percolation of snowmelt or rainfall, from the underlying melting ice, via capillary action – and their phase changes have not been taken into account. Rather, any water is assumed to run off immediately, without ponding or undergoing phase changes, both of which would influence the thermal properties of the debris.

Both field observations and laboratory experiments indicate that debris covers can be partially or entirely saturated at times during the ablation season, depending on the thickness and environmental conditions, with a minimum of a saturated region adjacent to the interface if the underlying ice is at the melting point (e.g. Nakawo and Young, 1981; Conway and Rasmussen, 2000; Kayastha et al., 2000; Reznichenko et al., 2010; Nicholson and Benn, 2012). The presence of interstitial water and ice modifies the thermal properties of the debris layer, particularly during transition seasons (e.g. Conway and Rasmussen, 2000; Nicholson and Benn, 2012). Percolation of rain or melt water through a debris layer, which can reach as high as 75 % of the total input (Sakai et al., 2004), can influence the thermal regime by heat advection (Reznichenko et al., 2010), and by providing a source of moisture for evaporation that cools the debris and therefore reduces heat transmission to the ice.

Water vapour exchanges between the surface and the overlying atmosphere influence the surface energy balance and have been observed to be non-negligible at times. Sakai et al. (2004). estimated that the ablation calculated by an energy balance approach that neglects the latent heat flux, QL, would provide an overestimate by 100 %, since the lowering effect of QL on surface temperature would not be captured. During the ablation season on the Miage glacier in the Italian Alps, Brock et al. (2010) calculate large spikes in QL, of up to $-800\,\mathrm{W\,m^{-2}}$, that coincide with daytime rainfall events on the heated debris surface. Furthermore, while they estimate that energy inputs due to condensation or deposition were negligible, ground frosts were observed to be weekly or bi-weekly occurrences in the upper parts of the glacier, which may slow early daytime heating of the debris layer. Given the clear influence of moisture on the surface

TCD
8, 1589–1629, 2014

energy balance and the subsurface thermal regime, there is a need to develop a treatment for moisture fluxes into and within the debris layer, as well as for phase changes that would allow for a variation in the thermal properties and energy sources and sinks of the debris layer with depth and time.

In this paper, we explore the utility of a single-reservoir scheme for parameterizing moisture fluxes and phase changes in a glacier debris layer that has been incorporated into a glacier climatic mass balance model. We exploit a short period of available in situ measurements over supraglacial debris to evaluate the model performance during an ablation season, with a second simulation of a fall season to fully demonstrate the capabilities of the model. Within the context of the simplified parameterization, we show the influence of moisture on heat transfer in the debris layer, its physical properties, and sub-debris ice melt, as well as assess the scale of the impact of phase changes. The eventual goal of this work is to incorporate the debris modifications into an interactively coupled modelling system of the atmosphere and alpine glaciers at the regional scale (Collier et al., 2013). The inclusion of debris is essential for (1) accurately capturing surface conditions over debris-covered glaciers and, therefore, atmosphere-glacier feedbacks, and (2) rigorously assessing regional climatic influences on the CMB of debris-covered glaciers.

2 Methods

2.1 Glacier CMB model

The debris-free version of the glacier CMB model is described fully by Mölg et al. (2008, 2009, 2012) and Collier et al. (2013). The model solves the surface energy balance equation to determine the energy available for melt and other mass fluxes, given by

$$S\downarrow \cdot (1-\alpha) + \epsilon \cdot (L\downarrow - \sigma \cdot T_{\mathrm{SFC}}^4) + \mathrm{QS} + \mathrm{QL} + \mathrm{QG} + \mathrm{QPRC} = F_{\mathrm{NET}} \quad (1)$$

TCD
8, 1589–1629, 2014

in which the terms correspond to, from left to right, net short- and long-wave radiation, turbulent fluxes of sensible and latent heat, the ground heat flux (composed of conduction and penetrating shortwave radiation) and the heat flux from precipitation. Following the convention in mass balance modelling, fluxes are defined as positive when energy transfer is to the surface. The residual energy flux, F_{NET}, constitutes the energy available for melt if the surface temperature has reached the melting point. The specific mass balance is calculated from solid precipitation, surface vapour fluxes, surface and subsurface melt, and refreeze of liquid water (melt and rain) in the snowpack. The model treats numerous additional processes, including the evolution of surface albedo and roughness based on snow depth and age; snowpack compaction and densification by refreeze; and the influence of penetrating solar radiation, refreeze and conduction on the englacial temperature distribution. Physical parameter values for snow and ice are provided in Table 1.

2.2 Inclusion of debris

For this study, the glacier CMB model has been modified to include a treatment for supraglacial debris according to two cases: (1) one with no treatment of moisture fluxes or phase changes in the debris layer, congruent with previous studies (CMB-DRY), and (2) one that introduces a single reservoir to parameterize the moisture content of the debris layer and its phase and also includes a latent heat flux calculation (CMB-RES). The simulations are performed as point simulations, due to the availability of both meteorological-forcing and evaluation data at only one location.

Both versions of the CMB model prognose the englacial temperature distribution using the heat equation,

$$\rho c \frac{\partial T}{\partial t} = \frac{\partial}{\partial z}\left(k \frac{\partial T}{\partial z}\right) + \frac{\partial Q}{\partial z} \quad (2)$$

where ρ is density $\mathrm{kg\,m^{-3}}$, c is the specific heat capacity $\mathrm{J\,kg^{-1}\,K^{-1}}$, T is temperature K, k is the thermal conductivity $\mathrm{W\,m^{-1}\,K^{-1}}$, and $Q\,\mathrm{W\,m^{-2}}$ is a heat flux due to any non-

TCD
8, 1589–1629, 2014

conductive processes. For these simulations, the numerical scheme used to solve Eq. (2) was updated from a centred-difference approach to a Crank–Nicholson scheme, which was solved following Smith (1985). The greater stability of the numerics permits the subsurface layer spacing to be decreased to 1 cm throughout the debris from 10 cm previously, consistent with the small number of previous studies that explicitly model heat conduction in the debris (e.g. Reid and Brock, 2010; Reid et al., 2012; Lejeune et al., 2013), rather than assume that the temperature gradient is approximately linear. The model contains variable layer spacing in the snowpack and underlying ice.

With the exception of Lejeune et al. (2013), the ice temperature in previous modelling has been assumed to be at the melting point, due to the focus on the ablation season (e.g. Nicholson and Benn, 2006; Reid and Brock, 2010). Although this assumption has been validated by field measurements (e.g. Conway and Rasmussen, 2000; Brock et al., 2010), it limits the temporal applicability of the model and may contribute to overestimation of night-time surface temperature when the overlying air temperature drops below the melting point (Reid and Brock, 2010). The CMB models explicitly simulate heat conduction throughout the column, and the ice temperature at all levels except the bottom boundary is a prognostic variable.

Previous modelling studies of debris-covered glaciers have employed an iterative approach to prognosing surface temperature, with the solution yielding zero residual flux in the surface energy balance (e.g. Nicholson and Benn, 2006; Reid and Brock, 2010; Reid et al., 2012; Zhang et al., 2011). The glacier CMB model in this study instead employs the method of Klok and Oerlemans (2002), in which the residual flux is distributed over a representative surface layer. This parameter is defined as the depth at which the amplitude of the daily diurnal temperature cycle reaches 5 % of its surface amplitude. For this study, it was determined from heat diffusion modelling for a column of ice and overlying debris of the appropriate thickness under sinusoidal temperature forcing.

The important physical properties of the glacier subsurface in Eq. (2) are non-uniform with depth. Specific to the debris, the properties of each 1 cm layer are a weighted aver-

TCD
8, 1589–1629, 2014

age of the whole-rock values and the content of the pore space (Table 1) as determined by an assumed porosity function. For CMB-DRY, the pore space contains only air, while for CMB-RES the weighted average also considers the bulk water and ice content of the debris.

The turbulent fluxes of sensible (both models) and latent (CMB-RES) heat are corrected for atmospheric stability, as is standard in glacier energy balance modelling (e.g. Braithwaite, 1995; Reid and Brock, 2010). To be consistent with previous studies of debris-covered glaciers, we set the latent heat flux to zero for CMB-DRY, as no measurements of surface relative humidity are available. In order to calculate the latent heat flux between the debris and the atmosphere in CMB-RES, the surface vapour pressure is required but unknown. For the case study described in Sect. 2.3, an automatic weather station (AWS) measured relative humidity at a height of $z_{\mathrm{air}} = 2.16\,\mathrm{m}$, from which the partial vapour pressure was calculated. The partial density of water vapour is then obtained from,

$$e_{\mathrm{air}} = \rho_{\mathrm{air}}^{\mathrm{vap}} R_{\mathrm{v}} T_{\mathrm{air}} \tag{3}$$

where the symbols correspond to, from left to right, the air's water vapour partial pressure, the partial density of water vapour, the specific gas constant for water vapour ($461.5\,\mathrm{J\,kg^{-1}\,K^{-1}}$), and the air temperature at a height of z_{air}. In this study, we assumed that $\rho_{\mathrm{air}}^{\mathrm{vap}}$ is constant between the sensor and the surface of the debris layer, i.e., that water vapour in the atmospheric surface layer is well mixed. The vapour pressure at the surface is therefore given by,

$$e_{\mathrm{sfc}}^{*} = \frac{e_{\mathrm{air}} T_{\mathrm{sfc}}}{T_{\mathrm{air}}} \tag{4}$$

A latent heat flux therefore arises, due to the vapour pressure gradient that results from the temperature difference between the surface and zair.

For CMB-RES, a single-reservoir scheme for moisture accumulation and phase changes is introduced (Fig. 1). The reservoir depth is calculated from the total debris porosity multiplied by the debris thickness. Liquid water, from rainfall or melt of the

TCD
8, 1589–1629, 2014

overlying snowpack, instantly infiltrates the reservoir. In addition, when the ice-debris interface reaches the melting point, a minimum debris water content of $2\,\mathrm{kg\,m^{-2}}$ is imposed to reflect field observations of a basal saturated layer during the ablation season. The location of the water and/or ice in the debris is not prognosed; rather, the water and ice are assumed to occupy the lowest debris layers, adjacent to the glacier ice. Both melt and refreeze are computed using the bulk temperature and physical properties of saturated or ice-filled debris layers. We also account for horizontal drainage of debris water, using a runoff timescale that is a linear function of terrain slope that varies from 1 to $0\,\mathrm{h^{-1}}$ between 0° and 90°, which is a simplistic representation of runoff timescales (Reijmer and Hock, 2008). Finally, although CMB-RES predicts water and ice in the reservoir, they are not included in the mass balance calculation so as to allow for a more direct comparison, between CMB-RES and CMB-DRY, of the influence of including a latent heat flux. However, the exclusion of the water and ice has a negligible influence on the total accumulated mass balance, as quantified in Sect. 3.

When the debris is exposed at the surface, the final calculation of the surface vapour pressure, e_{sfc}, includes a linear correction towards saturation, $e_{\mathrm{sfc\,sat}}$, at T_{sfc} according to,

$$e_{\mathrm{sfc}} = e^{*}_{\mathrm{sfc}} + \left(e_{\mathrm{sfc\,sat}} - e^{*}_{\mathrm{sfc}}\right) \cdot F_{\mathrm{res}} \tag{5}$$

where is the initial guess in Eq. (4) and F_{res} is the fractional fullness of the single reservoir with water and ice. Therefore, the surface vapour pressure is a function of the moisture content of the reservoir rather than a wetted debris surface: as the bucket fills from infiltration of rainfall or snowmelt, F_{res} increases and e_{sfc} approaches saturation. In reality, water vapour fluxes occur at the saturated horizon, either on the surface or within the debris layer. However, due to the complexity of the determining the location of the saturated horizon as well as accounting for additional processes, such as wind-driven transport of vapour within the debris, we employ this simplification.

TCD
8, 1589–1629, 2014

2.3 Miage Glacier case study

The study area is the Miage glacier in the Italian Alps (45° 47′ N, 6° 52′ E; Fig. 2). This glacier was selected due to the availability of meteorological data from an AWS, located on the lower, debris-covered part of the glacier at an elevation of 2030 m a.s.l., where the thickness is 23 cm. At the surface, the debris is composed mainly of coarse gravel and cobbles, ranging in size from a few centimetres to 25 cm in size, with occasional larger rocks, one to two meters in size. The AWS site was deliberately chosen to be upwind from any nearby large boulders.

We perform two simulations, one for summer 2008 and one for fall 2011. The former covers the period of 25 June–11 August 2008 with the first 25 days discarded as model spin-up time. For much of the 2008 simulation, the AWS provided hourly values of air temperature, vapor pressure, wind speed, and incoming short- and long-wave radiation (Fig. 3). However, during the spin-up period, wind speed and incoming longwave radiation were missing due to a programming error. To provide this missing data, wind speed was generated synthetically using the hourly average from the measured data during the evaluation period. Incoming longwave radiation was obtained from the ERA Interim reanalysis (0.75° × 0.75° resolution; Dee et al., 2011), with data from the closest model grid cell in the reanalysis used after being interpolated from 12 hourly to hourly reference points. For the time period where both ERA Interim and AWS data overlap (20 July–11 August 2008), the mean deviation and mean absolute deviation (ERA minus AWS) are 12.6 and 34.7 $W m^{-2}$, which likely arises due to the difference between modelled and real terrain height of −450 m). Lastly, a rain gauge was not installed at the AWS site in 2008. We therefore used input data from another AWS located 4 km away (denoted as AWS2 in Fig. 2) and assumed that they were representative of conditions at the AWS on the Miage glacier.

The 2008 simulation is intended to coincide with a supplementary field measurement program. Between 20 July and 11 August, surface temperature and the turbulent fluxes of latent and sensible heat were measured. The first field was measured with

TCD
8, 1589–1629, 2014

a CNR1 radiation sensor (Kipp & Zonen, Delft, the Netherlands), while the latter two fluxes were measured by an eddy covariance (EC) station. This comprised a CSAT three-dimensional sonic anemometer and KH2O Krypton Hygrometer (both Campbell Scientific Limited, Shepshed, UK), installed at a height of 2 m above the debris surface. These sensors measured three components of turbulent wind velocity, virtual temperature and water vapour concentrations at an interval of 50 ms. Raw data were processed using Campbell Scientific OPEC software, which included a "WPL" correction for density effects (Webb et al., 1980) and 30 min averages of the 50 ms scans were stored. The data were filtered for outliers using three times their standard deviation before being used for evaluation (Brock et al., 2010). Surface temperature was calculated from the upwelling longwave radiation recorded by the CNR1, using an emissivity of 0.94. The AWS tripod provided a stable platform on the slowly melting glacier surface, although the possibility of tilting of the instrument mast cannot be avoided. These measurements provide a unique data set with which to evaluate the CMB models using direct measurement of turbulence in the surface atmospheric layer above a debris-covered glacier.

However, the 2008 simulation does not contain any phase changes, since the air temperature remains above freezing (cf. Fig. 3a). In order to fully demonstrate the model capabilities, we perform a second simulation from 6 June–11 October 2011 discarding all but the period of 14 September–11 October as model spin-up time, due to the focus on the influence of phase changes. We focus our analysis on two freezing events, from 18–19 September and 7–9 October 2011. Incoming long-wave radiation, precipitation and mean wind speed are available hourly from the AWS (forcing data not shown), and measured surface temperature data, estimated from the upwelling longwave radiation recorded by the CNR1 are available for model evaluation.

A final forcing variable for the calculation of the debris surface energy balance, surface pressure, was missing for both the 2008 and 2011 simulations. These data were obtained from the ERA Interim reanalysis, at 6 hourly temporal resolution, and again from the closest grid cell. A correction applied for the difference between the real and

TCD
8, 1589–1629, 2014

modelled terrain height using the hypsometric equation, assuming a linear temperature gradient calculated from the AWS and the air temperature on the first model level in ERA interim.

The subsurface layer spacing for both simulations is provided in Table 2. The glacier subsurface temperature profile was initialized at the melting point, and the lower boundary value, located at a depth of 9.0 m in the ice, was set at 268.5 K, based on previous applications of the clean version of the CMB model (e.g. Mölg et al., 2012; Collier et al., 2013). Uncertainties in the temperature initialization were addressed by the inclusion of long spin-up periods. Subsurface heating due to penetrating shortwave radiation is not considered when the debris is exposed at the surface (e.g. Reid and Brock, 2010).

To ascertain the appropriate depth of the representative surface layer, we modelled heat diffusion for a column with 23 cm of dry debris overlying ice with the same treatment of physical and thermal properties discussed in Sect. 2.2. We forced the purely diffusive simulation with a sinusoidal daily temperature cycle, using an amplitude (22 K) and offset (13 K) consistent with the available, radiatively measured surface temperature data between 20 July and 11 August. The depth at which the diurnal amplitude reached 5 % of its surface value fell between 21 and 22 cm and was closer to the latter value.

For both CMB-DRY and CMB-RES, we assumed that the debris porosity is a linear function of depth in the debris, decreasing from 60 % at the surface down to 20 % at the debris-ice interface, based on field measurements on the Miage glacier by the authors, and observations of other glacier debris covers (Nicholson and Benn, 2012). The thermal and physical properties of the column were also either taken from field measurements or from specified values used in previous modelling studies of this glacier (Reid and Brock, 2010).

A slope of 7° at the AWS gives a runoff timescale of $0.92\,h^{-1}$. This simple representation of runoff timescales does not consider contributions from upslope regions in the glacier; however, we feel that this is an appropriate first step given that horizontal transport of water within the debris is poorly constrained and no measurements are

TCD
8, 1589–1629, 2014

available. The results are relatively insensitive to the value of the runoff timescale. Varying the terrain slope from 4° and 10° (equivalent to changing the runoff timescale by approximately ±4 %) results in changes in total accumulated mass balance and sub-debris ice melt of less than 0.6 % and 0.2 %, respectively, in 2008 and of 1.3 % and 0.5 % in 2011.

Finally, although the CMB models are evaluated against a short summer period in 2008 and in fall 2011, they are applicable throughout the annual cycle and to glaciers of any temperature regime, as illustrated in Fig. 1.

3 Results

3.1 Comparison with in situ measurements

The surface temperatures (T_{sfc}) simulated by CMB-DRY and CMB-RES are in good agreement with measurements for both the 2008 and 2011 simulations (Fig. 4a and d). In 2008, the models tend to overestimate the magnitude of night-time radiative cooling, leading to a negative mean deviation (MD; Table 3); however, for both simulations, the models reproduce the diurnal cycle and its variability well. The CMB models also capture the variability of the sensible heat flux (QS), but the simulated magnitude of heat transfer to the overlying atmosphere is much larger than reported by the EC station. The overestimation of QS for the CMB-DRY run is, in part, attributable to the lack of latent heat flux (QL), which means that an average energy loss of 24 $W m^{-2}$ is not captured (Fig. 4c). CMB-RES has a greatly reduced but still non-negligible bias in QS, again, in part, because evaporative cooling is underestimated, by $\sim 9\,W m^{-2}$ on average.

The relatively small latent heat flux compared with the EC data results from the approach used to estimate surface vapour pressure (cf. Sect. 2.2), which produces only a small gradient between the surface and overlying air (on average, $-0.2\,hPa\,m^{-1}$; Fig. 5a). Therefore, the influence of the single-reservoir parameterization on the total

TCD
8, 1589–1629, 2014

accumulated ablation between 20 July and 11 August 2008 is small: it increases from 198.1 kg m^{-2} in CMB-DRY to 208.5 kg m^{-2} in CMB-RES (Fig. 5b). These values are equivalent to an ablation rate of approximately 10 mm w.e. d^{-1}, which is in order of magnitude agreement with the value of 22 mm w.e. d^{-1} reported by Fyffe et al. (2012), based on the entire ablation seasons of 2010 and 2011.

3.2 Modelling insights from the 2008 simulation

The mass fluxes underlying the simulated mass balance signal are determined by the surface energy balance, whose daily-mean components are shown in Fig. 6a for CMB-RES. Energy receipt mainly through net shortwave radiation is generally counteracted by energy losses though net longwave radiation, heat conduction (QC), and turbulent fluxes of latent (QL) and sensible (QS) heat. During or shortly after rainfall events, such as those on 31 July and 5–6 August, QS is less negative. The heat flux to the debris surface from precipitation (QPRC) has an average value of −14.8 W m^{-2} during rainfall events. However, since the precipitation temperature is assumed to be the same as T_{air}, QPRC is a stronger energy sink for daytime rainfall. These energy fluxes produce ablation that is dominated by sub-debris ice melt and evaporation over the evaluation period, although there are small mass inputs from condensation, particularly during rainfall events (Fig. 6b; Table 4). Surface melt, refreeze, sublimation and deposition are zero, since there is no solid precipitation and both the debris surface and bulk temperatures remain above the melting point.

Compared with CMB-DRY, CMB-RES simulates slightly lower daytime debris-surface temperatures, as a result of heat extraction by QL (cf. Fig. 4a, Table 3). Energy transfer to the ice-debris interface is therefore also lower, contributing to a small reduction in sub-debris ice melt, of 4.6 W m^{-2} (Table 4). However, the reduction in melt is more than compensated for by surface vapour fluxes, with a total of 15.4 kg m^{-2} of evaporation over the evaluation period. Evaporation dominates during the day (96 % of the total), while smaller amounts of condensation occur mainly at night (61 % of the total) or in the early morning.

TCD
8, 1589–1629, 2014

Water accumulates in the supraglacial debris after rainfall events and then is removed, mainly by horizontal drainage but also by evaporation (Fig. 7). The total accumulated mass balance is negligibly altered if changes in debris water content are considered in addition to surface vapour fluxes (a further ablation of 0.2 kg m^{-2}). Both models treat the physical properties of the debris layer – thermal conductivity, density, and specific heat capacity – as functions of depth. Figure 8a–c shows their variation with depth for "dry" conditions, when there is no significant debris water storage, and for "wet" conditions, when there is significant water present as a result of rainfall. "Dry" conditions prevail, comprising 76 % of the evaluation period (Fig. 8d–f), under which tcd and d increase while dcp decreases as the porosity decreases with depth. The debris physical properties in CMB-DRY and CMB-RES are the same, with the exception of the bottom layer adjacent to the ice-debris interface, which remains fully saturated as a result of the ice-melt source term described in Sect. 2.2. Meltwater present in this layer acts to increase all three properties compared with CMB-DRY. Rainfall events and the associated moisture storage extend this influence upwards through the debris layer, with a significant alteration to the fully saturated layers (spanning the depth between 20 and 23 cm for the "wet" sample time slice) and a smaller effect on the partially saturated layer (at a depth of 19 cm). The debris specific heat capacity is the most strongly affected physical property, since the value of water is approximately four times that of air (4181 vs. 1005 J kg^{-1} K^{-1}).

The effective thermal diffusivity of the debris is inversely proportional to the specific heat capacity and the debris density. Increases in both of these quantities, but particularly that of dcp, reduce heat diffusion over affected layers compared with the dry model. Therefore, in combination with heat extraction by QL, the change in subsurface physical properties reduces the amplitude and depth-penetration of the diurnal temperature cycle in the debris layer (Fig. 9). Fluctuations in the magnitude of QL has a correlation coefficient of 0.93 with the temperature difference between CMB-RES and CMB-DRY (TRES-DRY) in the top 5 cm of the debris, while reductions in the effective thermal diffusivity have a correlation coefficient of 0.55 with TRES-DRY of saturated

TCD
8, 1589–1629, 2014

layers. However, since the entire column is initialized at the melting point and the air temperature remains positive over the entire simulation, the influence on sub-debris ice melt is relatively small: the percent change in sub-debris ice melt is −2.6 % under "dry" conditions vs. −1.6 % under "wet" conditions.

3.3 Impact of phase changes in the 2011 simulation

Two freezing events occur during the 2011 simulation, between 18 September 23:00 LT–19 September 14:00 LT and between 7 October 9:00 LT–9 October 9:00 LT, at the tail end of two precipitation events with sub-zero air temperatures (cf. Fig. 4d). Net longwave and shortwave radiation are reduced, due to cooler surface temperatures and to small amounts of snowfall that increase the surface albedo (Fig. 10a). Immediate melt of the thin overlying snow cover (< 0.5 cm) and infiltration of rainfall at the beginning of the precipitation event provide the source water for refreeze in the debris layer (Figs. 10b and 11a). Refreeze occurs overnight and during the early-to-mid day, while the ice melts partially or fully in the mid-to-late afternoon and evening. Small amounts of evaporation and sublimation accompany periods of melt and refreeze, respectively (Table 5).

The bulk presence of liquid water and ice in the debris layer influences the vertical temperature profile in three ways (Fig. 11b and c). First, the effective thermal diffusivity of moist or frozen layers is reduced compared with the dry debris; therefore, the cooling wave reaches the debris-ice interface more slowly (meaning that highest affected layer shows a warm differential earlier than lower layers). Second, latent heat release due to refreeze warms the subsurface, on average by 0.4 K but exceeding 1 K for the hourly time steps with the greatest refreeze. Third, the presence of ice in the lowest layers delays daytime heating of the debris compared with CMB-DRY until the ice has melted. The accumulated mass balance between 14 September–11 October 2011 is $-132.3\,\mathrm{kg\,m^{-2}}$ for CMB-DRY and $-136.1\,\mathrm{kg\,m^{-2}}$ for CMB-RES. Changes in water and ice storage again have a nearly negligible impact on simulated mass balance, resulting in an increase of total accumulated ablation of $0.2\,\mathrm{kg\,m^{-2}}$.

TCD
8, 1589–1629, 2014

4 Discussion

Both the observed and simulated QL are non-zero over the simulation period, with regular fluctuations on the order of 10 $W m^{-2}$ and occasional spikes of more than $\pm 100\ W m^{-2}$ (after filtering, as described in Sect. 2.3; cf. Fig. 4c). Among other sources of error, intense precipitation can cause erroneous spikes in the EC measurements as a result of raindrops interfering with the path of the sonic anemometer (e.g. Aubinet et al., 2012). However, of the 15 occurrences of such spikes in the EC data, only two occur during or within one hour of precipitation. In combination with previously reported large QL values, of up to $-800\ W m^{-2}$ during rainfall events on heated debris (Brock et al., 2010), neglecting QL in a surface energy balance calculation can be inappropriate, and under certain meteorological conditions is likely to have a significant impact on the calculated energy fluxes.

Rounce and McKinney (2014) also emphasize the importance of QL, in their case in a steady-state energy balance model used to retrieve thermal resistances from satellite data. For their formulation of QL, the "surface" vapour pressure was determined from the saturation value at the temperature at a depth of 10 cm (their Eq. 6), which was inferred to be the approximate boundary between wet and dry debris. Testing this formulation for saturation vapor pressure at our model surface in the 2008 simulation with CMB-RES results in strong biases (MD = 95; MAD = 101 $W m^{-2}$) and a shift from QL as an energy sink to a gain, which is inconsistent with the EC data. However, their study points to the need for improving the representation of vapour fluxes in CMB-RES by accurately computing them at the position of the saturated horizon.

The magnitude of QS is sensitive to the choice of debris thickness, which was selected to be 0.23 m in this study based on a point measurement. However, the turbulent fluxes measured by the EC station respond to a larger area, with a variable and unknown debris thickness that likely ranges between 20–30 cm. The agreement between measured and modelled QS in 2008 is improved if the debris thickness in the models is reduced slightly. For example, using a thickness of 20 cm reduces the MD by

TCD
8, 1589–1629, 2014

$\sim 10\,W\,m^{-2}$ and the MAD by $\sim 5\,W\,m^{-2}$, for both CMB-RES and CMB-DRY. The stability correction of the turbulent fluxes may also need to be amended for applications over glacier debris, as in Foster et al. (2012) and Fyffe et al. (2014), to constrain the bulk Richardson number within reasonable limits when the surface temperature is high. Investigating the causes of discrepancies between modelled QS and that measured by the EC is not directly related to the inclusion of moisture in CMB-RES and is reserved for future work.

The difference in accumulated mass balance between CMB-RES and CMB-DRY is relatively small, for a point application in this configuration. However, scaled up to a larger debris-covered area, evaporation would represent a significant mass flux. For example, the daily mean evaporation rate was 0.8 mm w.e. in 2008 (June to early August 2008) and 0.6 mm w.e. in 2011 (June to September), which is comparable to values of reported over clean glaciers (e.g. Kaser, 1982). Over an ablation area of $4\,km^2$, this evaporation rate would result in water losses of approximately 0.12 and 0.25 Gt, respectively.

There are no ablation measurements available for either of the two simulation periods. However, if the debris thickness is arbitrarily varied from 1 to 20 cm under the same atmospheric forcing as the 2008 simulation, the CMB models produce daily-mean ablation rates as a function of debris thickness (Østrem curves) that are consistent with previously reported measurements (Mattson et al., 1993, ; Fig. 12). The critical thickness, or the thickness under which the ablation rate is equal to that of debris-free ice, is between 1–2 cm, which is on the low side of the range of 1.5–5 cm reported in empirical studies (e.g. Loomis, 1970; Fujii, 1977; Inoue and Yoshida, 1980; Mattson et al., 1993). CMB-RES produces a smaller rising limb of the Østrem curve than CMB-DRY, as a result of heat extraction by QL. To fully reproduce the rising limb of the Østrem curve, changes in the surface albedo as the debris cover becomes more continous may need to be accounted for, as in the albedo "patchiness" scheme introduced by Reid and Brock (2010).

TCD
8, 1589–1629, 2014

The magnitude and importance of liquid water inputs to glacier debris covers are poorly quantified. However, based on measurements of evaporation and percolation with a lysimeter, Sakai et al. (2004) found that while anywhere between 40–75 % of rainfall on a debris layer infiltrated, the resulting heat flux contributed only a small amount of energy ($4\,W\,m^{-2}$) to ice melt. Conversely, Reznichenko et al. (2010) found that debris permeability strongly controls the influence of rainwater percolation, such that sub-debris melt was enhanced by heat advection by rain in more permeable layers but completely inhibited by refreeze of interstitial water in less-permeable layers. Congruent with the simple nature of the single-reservoir parameterization that treats infiltration as instantaneous, the heat flux from precipitation is only applied at the surface in CMB-RES, and subsurface heat transport as a result of water percolation is not included.

5 Conclusions

In this paper, we introduced a new model for the surface energy balance and CMB of debris-covered glaciers that includes surface vapour fluxes and a single-reservoir parameterization for moisture infiltration and phase changes. Although the parameterization is a simplification of the complex moist physics of debris, our model is a novel attempt to treat moisture within glacier debris cover, and one that permits two important advances: (1) it incorporates the effects of ice and water on the physical and thermal properties of the debris and therefore on ice ablation, and (2) it includes an estimate of the moisture exchanges between the surface and the atmosphere.

The inclusion of the water vapour flux opens up avenues of future research. For example, distributed simulations are required to most rigorously investigate relevant scientific questions about debris-covered glaciers, such as projecting their behaviour and runoff under changing climate conditions. A key constraint in performing such simulations is obtaining forcing data, since the highly heterogeneous surface of debris-covered glaciers makes the spatial distribution of air temperature and winds uncertain.

TCD
8, 1589–1629, 2014

Current approaches, employing elevation-based extrapolation, appear to be inadequate (Reid et al., 2012). Interactive coupling with a high-resolution atmospheric model provides one solution; however, the conventional modelling approach would introduce errors due to the absence of moisture exchange between the surface and the atmosphere. In incorporating that flux, CMB-RES is a step towards more precisely computing glacier-atmosphere feedbacks within coupled surface-and-atmosphere modelling schemes and more accurately predicting alterations in freshwater budgets and other potential impacts of glacier change.

Acknowledgements. E. Collier was supported by a Natural Sciences and Engineering Research Council of Canada (NSERC) CGS-D award and an Alberta Ingenuity Graduate Student Scholarship. L. I. Nicholson was supported by an Austrian Science Fund (FWF) Elise Richter Award (#V309-N26). F. Maussion acknowledges support from the WET project (code 03G0804A), financed by the German Federal Ministry of Education and Research (BMBF). A. B. G. Bush acknowledges support from NSERC and from the Canadian Institute for Advanced Research. We also thank the Aosta Valley Autonomy Region for supplying meteorological data for the Lex Blanche station and P. Zöll for designing Fig. 1.

References

Aubinet, M., Vesala, T., and Papale, D. (Eds.): Eddy Covariance: a Practical Guide to Measurement and Data Analysis, Springer, Dordrecht, Heidelberg, London, New York, 1–19, 2012. 1605

Bhambri, R., Bolch, T., Chaujar, R. K., and Kulshreshtha, S. C.: Glacier changes in the Garhwal Himalaya, India, from 1968 to 2006 based on remote sensing, J. Glaciol., 57, 543–556, 2011. 1591

Bolch, T., Buchroithner, M., Pieczonka, T., and Kunert, A.: Planimetric and volumetric glacier changes in the Khumbu Himal, Nepal, since 1962 using Corona, Landsat TM and ASTER data, J. Glaciol., 54, 592–600, 2008. 1591

Braithwaite, R. J.: Aerodynamic stability and turbulent sensible-heat flux over a melting ice surface, the Greenland ice sheet, J. Glaciol., 41, 562–571, 1995. 1596

TCD
8, 1589–1629, 2014

Brock, B. W., Mihalcea, C., Kirkbride, M. P., Diolaiuti, G., Cutler, M. E., and Smiraglia, C.: Meteorology and surface energy fluxes in the 2005–2007 ablation seasons at the Miage debris-covered glacier, Mont Blanc Massif, Italian Alps. J. Geophys. Res., 115, D09106, doi:10.1029/2009JD013224, 2010. 1591, 1592, 1595, 1599, 1605

Collier, E., Mölg, T., Maussion, F., Scherer, D., Mayer, C., and Bush, A. B. G.: High-resolution interactive modelling of the mountain glacier–atmosphere interface: an application over the Karakoram, The Cryosphere, 7, 779–795, doi:10.5194/tc-7-779-2013, 2013. 1593, 1600

Conway, H. and Rasmussen, L. A.: Summer temperature profiles within supraglacial debris on Khumbu Glacier, Nepal, Debris-Covered Glaciers, IAHS PUBLICATION no. 264, 89–97, 2000. 1592, 1595

Dee, D. P., Uppala, S. M., Simmons, A. J., Berrisford, P., Poli, P., Kobayashi, S., Andrae, U., Balmaseda, M. A., Balsamo, G., Bauer, P., Bechtold, P., Beljaars, A. C. M., van de Berg, L., Bidlot, J., Bormann, N., Delsol, C., Dragani, R., Fuentes, M., Geer, A. J., Haimberger, L., Healy, S. B., Hersbach, H., Hlm, E. V., Isaksen, L., Kållberg, P., Köhler, M., Matricardi, M., McNally, A. P., Monge-Sanz, B. M., Morcrette, J.-J., Park, B.-K., Peubey, C., de Rosnay, P., Tavolato, C., Thpaut, J.-N., and Vitart, F.: The ERA-Interim reanalysis: configuration and performance of the data assimilation system, Q. J. Roy. Meteor. Soc., 137, 553–597, 2011. 1598

Foster, L. A., Brock, B. W., Cutler, M. E. J., and Diotri, F.: A physically based method for estimating supraglacial debris thickness from thermal band remote-sensing data, J. Glaciol., 58, 677–691, 2012. 1606

Fujii, Y.: Experiment on glacier ablation under a layer of debris cover, J. Japan. Soc. Snow Ice (Seppyo), 39, 20–21, 1977. 1591, 1606

Fyffe, C., Brock, B. W., Kirkbride, M. P., Mair, D. W. F., and Diotri, F.: The hydrology of a debris-covered glacier, the Miage Glacier, Italy, BHS Eleventh National Symposium, Hydrology for a changing world, Dundee, 9–11 July 2012, doi:10.7558/bhs.2012.ns19, 2012. 1602

Fyffe, C., Reid, T. D. Brock, B. W., Kirkbride, M. P., Diolaiuti, G., Smiraglia, C., and Diotri, F.: A distributed energy balance melt model of an alpine debris-covered glacier, J. Glaciol., in press, 2014. 1591, 1606

Han, H. D., Ding, Y. J., and Liu, S. Y.: A simple model to estimate ice ablation under a thick debris layer, J. Glaciol., 52, 528–536, 2006. 1591

Inoue, J. and Yoshida, M.: Ablation and heat exchange over the Khumbu Glacier, J. Japan. Soc. Snow Ice (Seppyo), 39, 7–14, 1980. 1591, 1606

TCD
8, 1589–1629, 2014

Kääb, A., Berthier, E., Nuth, C., Gardelle, J., and Arnaud, Y.: Contrasting patterns of early twenty-first-century glacier mass change in the Himalayas, Nature, 488, 495–498, 2012. 1591
Kaser, G.: Measurement of evaporation from snow, Arch. Met. Geoph. Biokl. Ser. B., 30, 333–340, 1982. 1606
Kayastha, R. B., Takeuchi, Y., Nakawo, M., and Ageta, Y.: Practical prediction of ice melting beneath various thickness of debris cover on Khumbu Glacier, Nepal using a positive degree-day factor, Symposium at Seattle 2000 – Debris-Covered Glaciers, IAHS Publ., 264, 71–81, 2000. 1591, 1592
Klok, E. J., and Oerlemans, J.: Model study of the spatial distribution of the energy and mass balance of Morteratschgletscher, Switzerland, J. Glaciol., 48, 505–518, 2002. 1595
Kraus, H.: An energy-balance model for ablation in mountainous areas, Snow and Ice-Symposium-Neiges et Glaces, August 1971, IAHS-AISH PUBLICATION no. 104, 1975. 1591
Lejeune, Y., Bertrand, J.-M., Wagnon, P., and Morin, S.: A physically based model of the year-round surface energy and mass balance of debris-covered glaciers, J. Glaciol., 59, 327–344, doi:10.3189/2013JoG12J149, 2013. 1591, 1595
Loomis, S. R.: Morphology and ablation processes on glacier ice, Assoc. Am. Geogr. Proc., 2, 88–92, 1970. 1591, 1606
Mattson, L. E., Gardner, J. S., and Young, G. J.: Ablation on debris covered glaciers: an example from the Rakhiot Glacier, Punjab, Himalaya, Snow and Glacier Hydrology, IAHS-IASH Publ., 218, 289–296, 1993. 1591, 1606
Mölg, T., Cullen, N. J., Hardy, D. R., Kaser, G., and Klok, E. J.: Mass balance of a slope glacier on Kilimanjaro and its sensitivity to climate, Int. J. Climatol., 28, 881–892, 2008. 1593
Mölg, T., Cullen, N. J., Hardy, D. R., Winkler, M., and Kaser, G.: Quantifying climate change in the tropical midtroposphere over East Africa from glacier shrinkage on Kilimanjaro, J. Climate, 22, 4162–4181, 2009. 1593
Mölg, T., Maussion, F., Yang, W., and Scherer, D.: The footprint of Asian monsoon dynamics in the mass and energy balance of a Tibetan glacier, The Cryosphere, 6, 1445–1461, doi:10.5194/tc-6-1445-2012, 2012. 1593, 1600
Nakawo, M. and Young, G. J.: Field experiments to determine the effect of a debris layer on ablation of glacier ice, Ann. Glaciol., 2, 85–91, 1981. 1591, 1592
Nakawo, M. and Young, G. J.: Estimate of glacier ablation under a debris layer from surface temperature and meteorological variables, J. Glaciol., 28, 29–34, 1982. 1591

TCD
8, 1589–1629, 2014

Nicholson, L. and Benn, D.: Calculating ice melt beneath a debris layer using meteorological data, J. Glaciol., 52, 463–470, 2006. 1591, 1595
Nicholson, L. and Benn, D.: Properties of natural supraglacial debris in relation to modelling sub-debris ice ablation, EPSL, 38, 490–501, 2012. 1592, 1600
Østrem, G.: Ice melting under a thin layer of moraine, and the existence of ice cores in moraine ridges, Geogr. Ann., 41, 228–230, 1959. 1591
Reid, T. D. and Brock, B. W.: An energy-balance model for debris-covered glaciers including heat conduction through the debris layer, J. Glaciol., 56, 903–916, 2010. 1591, 1592, 1595, 1596, 1600, 1606
Reid, T. D., Carenzo, M., Pellicciotti, F., and Brock, B. W.: Including debris cover effects in a distributed model of glacier ablation, J. Geophys. Res., 117, D18105, doi:10.1029/2012JD017795, 2012. 1591, 1592, 1595, 1608
Reijmer, C. H. and Hock, R.: Internal accumulation on Storglaciaren, Sweden, in a multi-layer snow model coupled to a distributed energy- and mass- balance model, J. Glaciol., 54, 61–71, 2008. 1597
Reznichenko, N., Davies, T., Shulmeister, J., and McSaveney, M.: Effects of debris on ice-surface melting rates: an experimental study, J. Glaciol., 56, 384–394, 2010. 1592, 1607
Rounce, D. R. and McKinney, D. C.: Thermal resistances in the Everest Area (Nepal Himalaya) derived from satellite imagery using a nonlinear energy balance model, The Cryosphere Discuss., 8, 887–918, doi:10.5194/tcd-8-887-2014, 2014. 1605
Sakai, A., Fujita, K., and Kubota, J.: Evaporation and percolation effect on melting at debris-covered Lirung Glacier, Nepal Himalayas, 1996, Bull. Glaciol. Res., 21, 9–15, 2004. 1592, 1607
Smith, G. D.: Numerical solution of partial differential equations: finite difference methods, 3rd edn., Oxford, Oxford University Press, 1985. 1595
Stokes, C. R., Popovnin, V., Aleynikov, A., Gurney, S. D., and Shahgedanova, M.: Recent glacier retreat in the Caucasus Mountains, Russia, and associated increase in supraglacial debris cover and supra-/proglacial lake development, Ann. Glaciol., 46, 195–203, 2007. 1591
Webb, E. K., Pearman, G. I., and Leuning, R.: Correction of flux measurements for density effects due to heat and water vapour transfer, Q. J. Roy. Meteor. Soc., 106, 85–100, 1980. 1599

TCD
8, 1589–1629, 2014

Zhang, Y., Fujita, K., Liu, S., Liu, Q., and Nuimura, T.: Distribution of debris thickness and its effect on ice melt at Hailuogou glacier, southeastern Tibetan Plateau, using in situ surveys and ASTER imagery, J. Glaciol., 57, 1147–1157, 2011. 1591, 1595

TCD
8, 1589–1629, 2014

Table 1. Physical parameter values used in the CMB models.

Density $kg\,m^{-3}$	
ice	915
whole rock	1496
water	1000
Specific heat capacity $J\,kg^{-1}\,K^{-1}$	
air	1005
ice	2106
whole rock	948
water	4181
Thermal conductivity $W\,m^{-1}\,K^{-1}$	
air	0.024
ice	2.51
whole rock	0.94
water	0.58
Surface roughness $[m^{-1}]$	
ice	0.001
debris	0.016
Albedo	
ice	0.34
firn	0.52
fresh snow	0.87
debris	0.13
Emissivity	
ice/snow	0.97
debris	0.94

TCD
8, 1589–1629, 2014

Table 2. Subsurface layer distribution and debris thickness used in this study.

Layers
Every 0.01 m from 0–0.24 m, 0.3, 0.4, 0.5, 0.8, 1.0, 1.4, 2.0, 3.0, 5.0, 7.0, 9.0 m
Debris thickness
0.23 m

TCD
8, 1589–1629, 2014

Table 3. Mean deviation (MD), mean absolute deviation (MAD), and R value for the evaluation variables of surface temperature (T_{sfc}), and the turbulent fluxes of sensible (QS) and latent heat (QL).

2008		CMB-DRY	CMB-RES
T_{sfc}	MD	−0.9	−1.4
	MAD	2.2	2.4
	R	0.96	0.96
QS	MD	−75.3	−59.3
	MAD	90.1	74.4
	R	0.88	0.89
QL	MD	23.9	3.9
	MAD	28.2	19.8
	R	–	0.5
2011		CMB-DRY	CMB-RES
T_{sfc}	MD	0.6	0.4
	MAD	1.2	1.1
	R	0.98	0.98

TCD
8, 1589–1629, 2014

Table 4. Average-energy and accumulated-mass fluxes at the surface over the 2008 simulation for CMB-RES and CMB-DRY.

average $W\,m^{-2}$	CMB-DRY	CMB-RES
net shortwave (SWnet)	237.6	237.6
net longwave (LWnet)	89.1	−86.6
conduction (QC)	−34.4	−33.4
sensible heat (QS)	−114.4	−98.3
latent heat (QL)	–	−20.1
precipitation (QPRC)	−1.0	−0.9
sum $kg\,m^{-2}$	CMB-DRY	CMB-RES
melt	–	0
refreeze	–	0
sublimation	–	0
deposition	–	0
evaporation	–	15.4
condensation	–	0.2
sub-debris ice melt	198.3	193.7

TCD
8, 1589–1629, 2014

Table 5. Average-energy and accumulated-mass fluxes at the surface over the 2011 simulation for CMB-RES and CMB-DRY.

average $W m^{-2}$	CMB-DRY	CMB-RES
net shortwave (SWnet)	132.7	132.7
net longwave (LWnet)	−77.8	−76.8
conduction (QC)	−18.9	−18.4
sensible heat (QS)	−32.8	−26.5
latent heat (QL)	−2.3	−10.4
precipitation (QPRC)	−0.1	0
sum $kg m^{-2}$	CMB-DRY	CMB-RES
melt	2.9	6.5
refreeze	0	3.6
sublimation	2.0	2.0
deposition	0.1	0.1
evaporation	–	7.7
condensation	–	0.2
sub-debris ice melt	132.4	128.8

TCD
8, 1589–1629, 2014

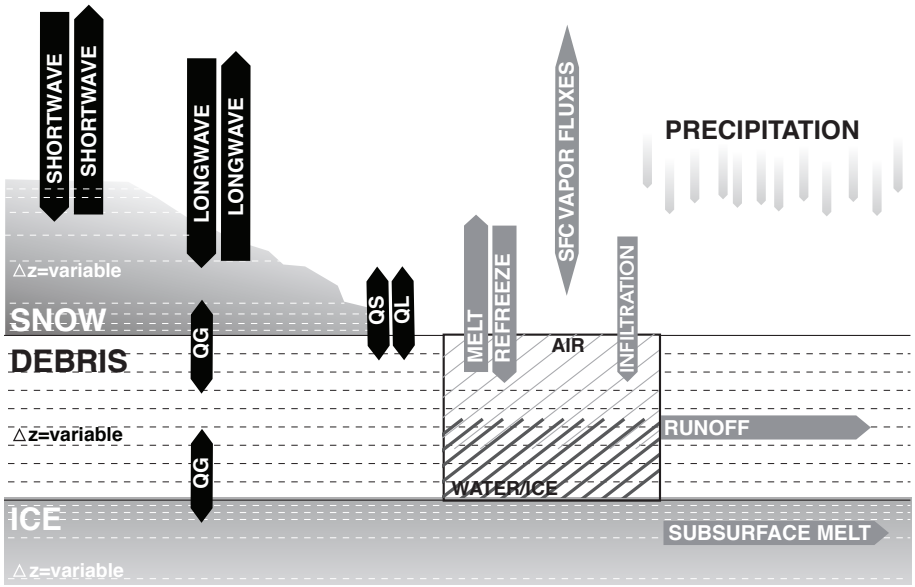

Fig. 1. Schematic of the CMB-RES model and its treatment of the debris moisture content and its phase.

TCD
8, 1589–1629, 2014

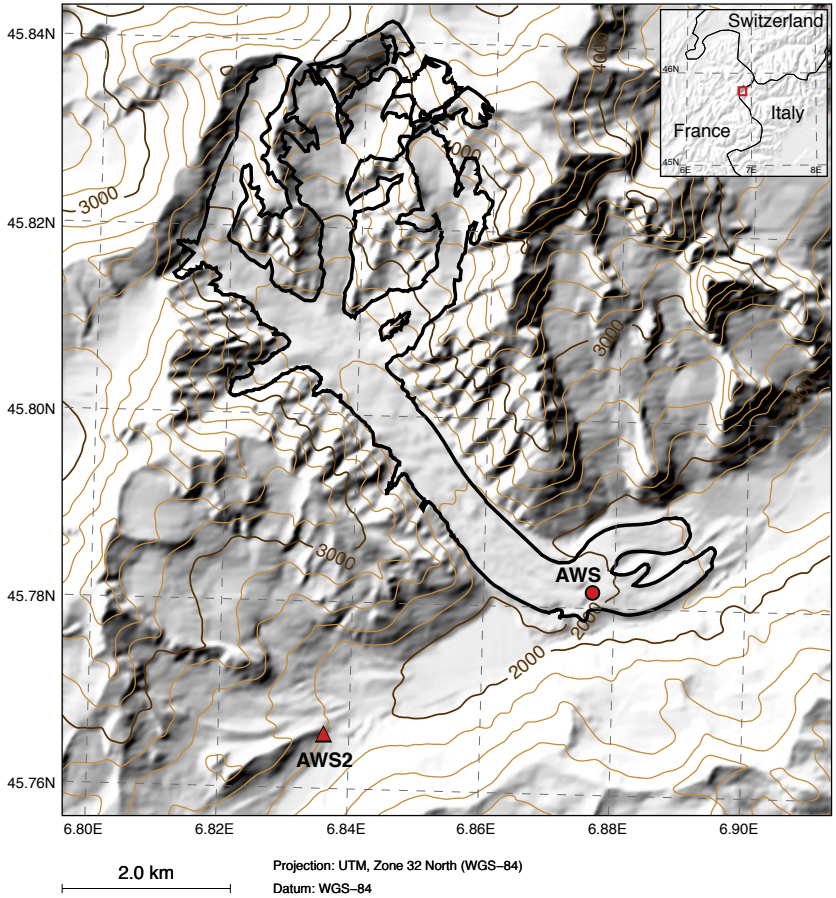

Fig. 2. Map showing the location of Miage glacier. The AWS located on the glacier is denoted with a red circle and the AWS2 from which precipitation data were obtained is shown by a red triangle.

TCD
8, 1589–1629, 2014

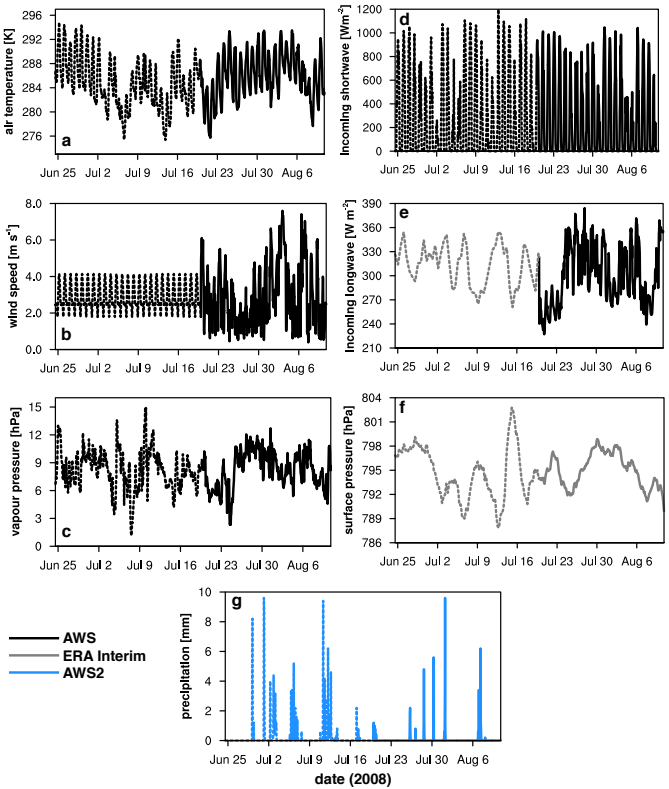

Fig. 3. Times series from the 2008 simulation of the forcing variables of **(a)** 2 m air temperature K, **(b)** wind speed $m\,s^{-1}$, **(c)** 2 m vapour pressure hPa, **(d)** incoming shortwave radiation $W\,m^{-2}$, **(e)** incoming longwave radiation $W\,m^{-2}$, **(f)** surface pressure hPa, and **(g)** precipitation mm. Data from the AWS on the Miage glacier are shown in black, from the second AWS (4 km away) in blue, and from the ERA Interim reanalysis in grey. Dashed curves indicate the discarded spin-up period, while solid curves indicate the simulation time.

TCD
8, 1589–1629, 2014

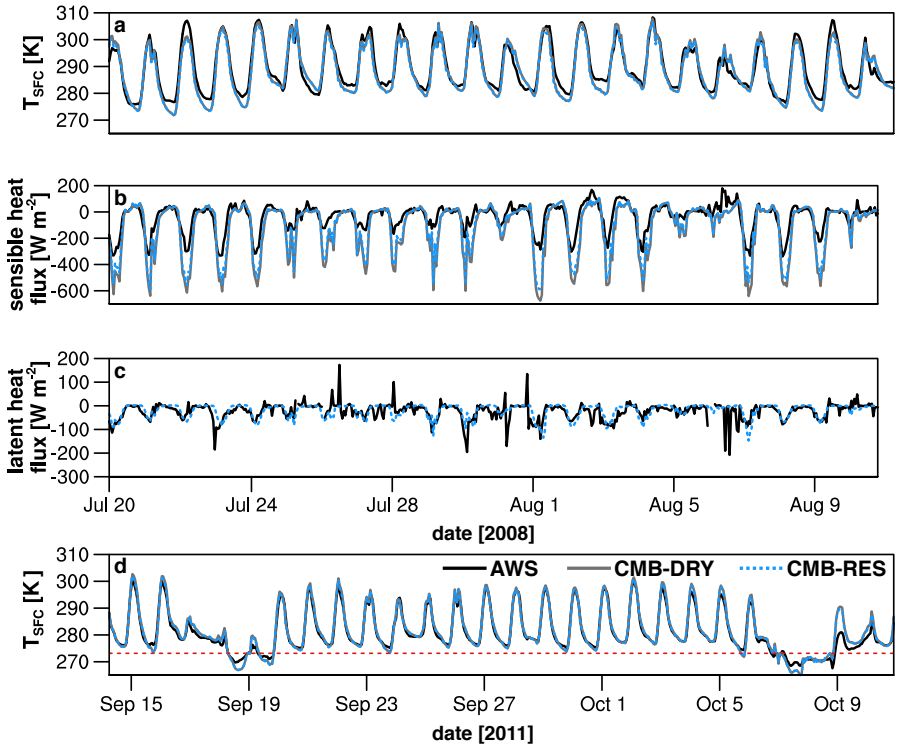

Fig. 4. Time series from the 2008 simulation of **(a)** debris surface temperature (T_{sfc}; K) and the turbulent fluxes of **(b)** sensible and **(c)** latent heat W m^{-2}, for measurements (black curve), CMB-DRY (dark grey curve), and CMB-RES (blue, dashed curve). **(d)** Same as panel a, but for the 2011 simulation. The horizontal dashed red line indicates the freezing point, 273.15 K.

TCD
8, 1589–1629, 2014

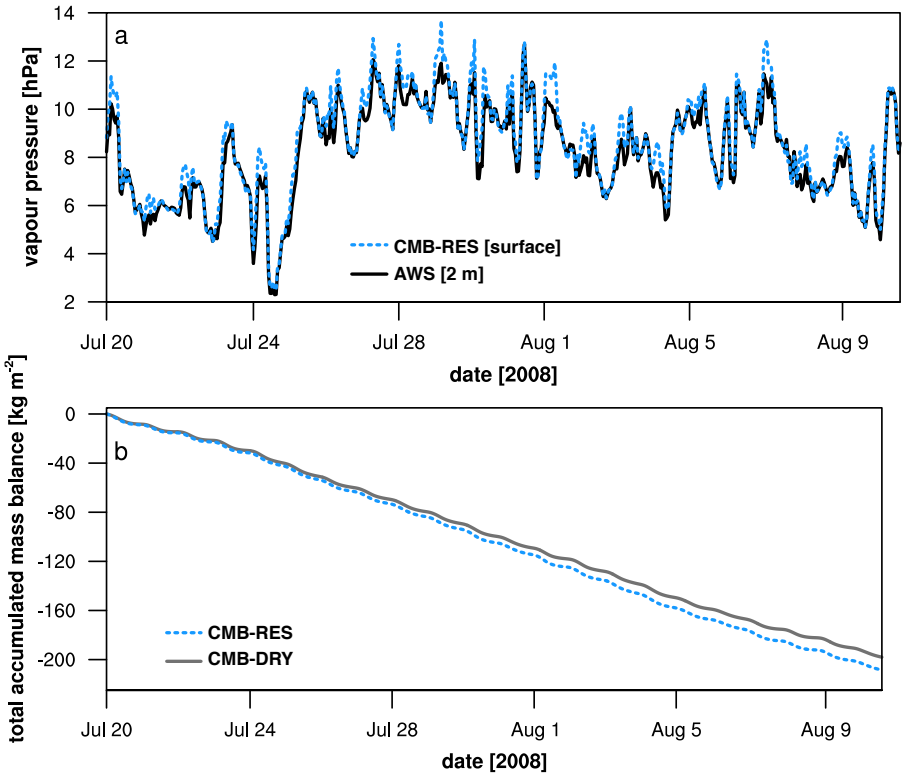

Fig. 5. Time series from the 2008 simulation of **(a)** surface (blue dashed curve) and 2 m air (black curve) vapour pressure in hPa in CMB-RES, and **(b)** total accumulated mass balance in kg m^{-2} for CMB-DRY (grey, solid curve) and CMB-RES (blue, dashed curve).

TCD
8, 1589–1629, 2014

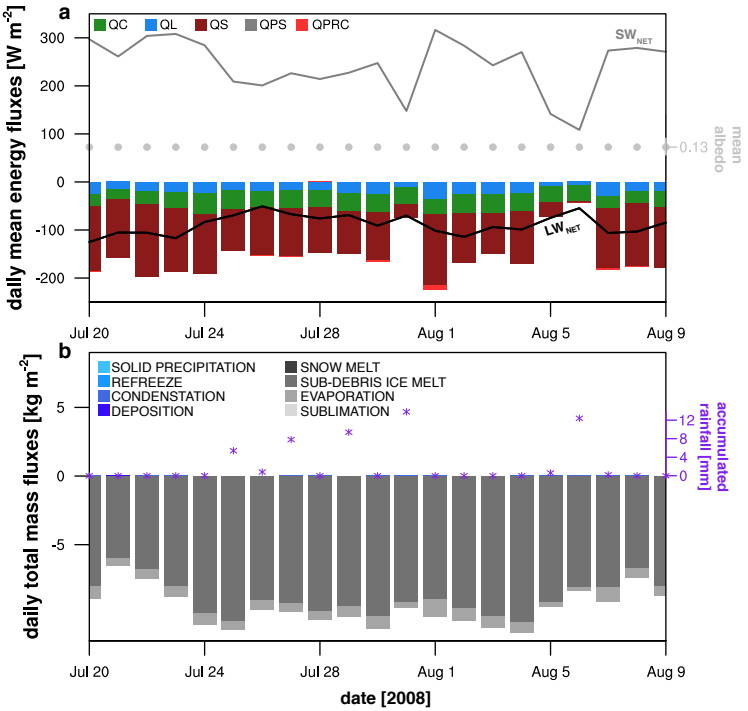

Fig. 6. CMB-RES values for **(a)** daily mean energy fluxes over the evaluation period in $\mathrm{W\,m^{-2}}$. The grey curve is net shortwave radiation, the black curve is net longwave radiation, and the grey dots show surface albedo, which remains constant at the debris value, since there is no solid precipitation. **(b)** Daily total mass fluxes in $\mathrm{kg\,m^{-2}}$. Peak daily values of evaporation and condensation are 1.3, and $3.4 \times 10^{-2}\,\mathrm{kg\,m^{-2}}$, respectively, although they are not visible. Note that while daily-accumulated rainfall is shown (purple asterisks), it is not technically a mass flux, since the mass balance calculation in CMB-RES does not account for debris water storage. Rather, this field is plotted to show its correspondence with other fields, such as net shortwave radiation.

TCD
8, 1589–1629, 2014

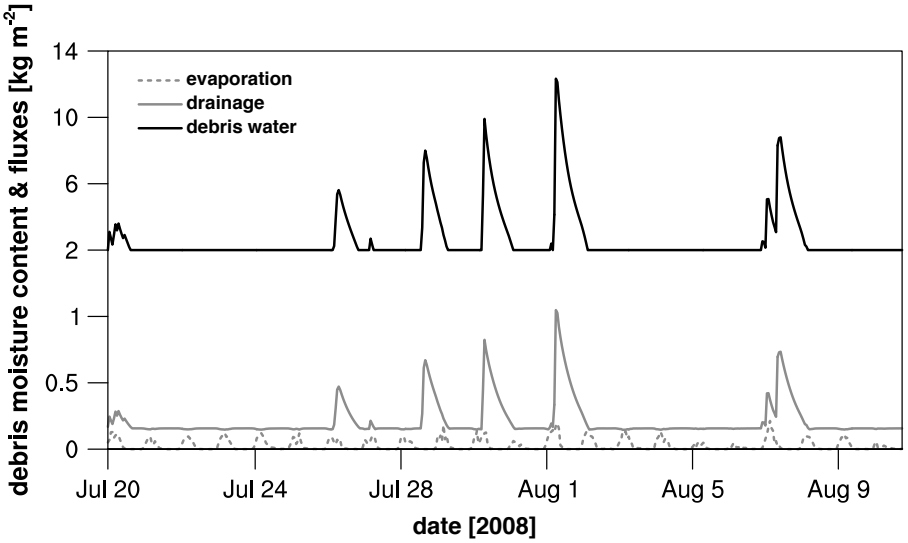

Fig. 7. Time series of total debris water content (black curve) as well as the two sources of debris water loss: horizontal drainage (solid grey curve) and evaporation (dashed grey curve). Units are kg m^{-2}.

TCD
8, 1589–1629, 2014

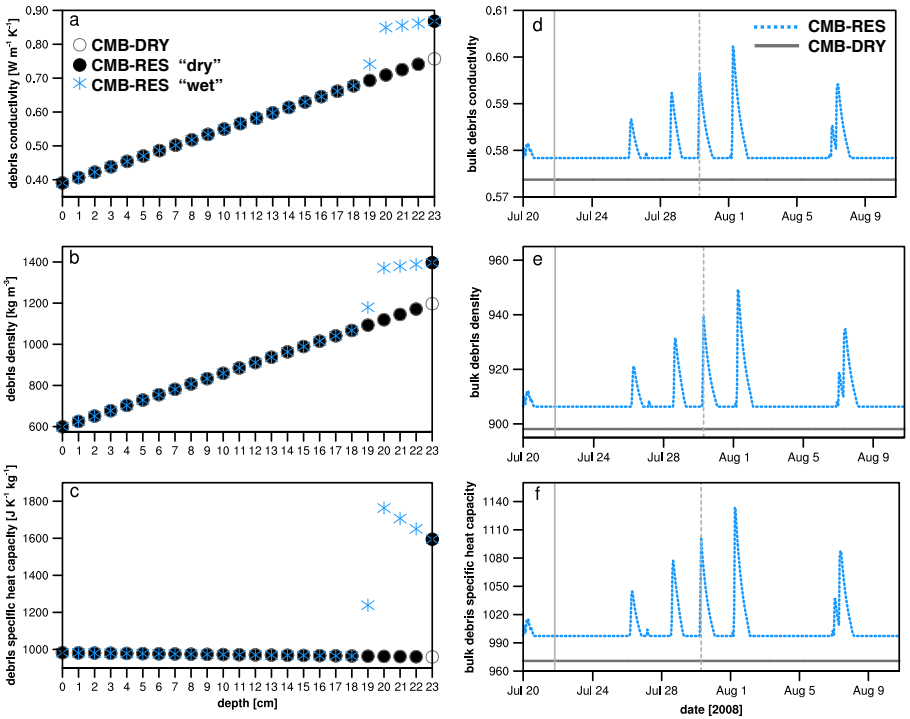

Fig. 8. Depth variation of **(a)** debris thermal conductivity $\mathrm{W\,m^{-1}\,K^{-1}}$, **(b)** density $\mathrm{kg\,m^{-3}}$, and **(c)** specific heat capacity $\mathrm{J\,kg^{-1}\,K^{-1}}$, shown for CMB-DRY in grey-unfilled circles and for CMB-RES in both black-filled circles ("dry" time slice) and blue asterisks ("wet" time slice). Time series of bulk values for these same properties are shown in panels **(d–f)** for CMB-RES in blue and CMB-DRY in grey. The locations of the "dry" and "wet" time slices are indicated by the first (solid grey) and second (dashed grey) reference lines on the x-axis, respectively.

TCD
8, 1589–1629, 2014

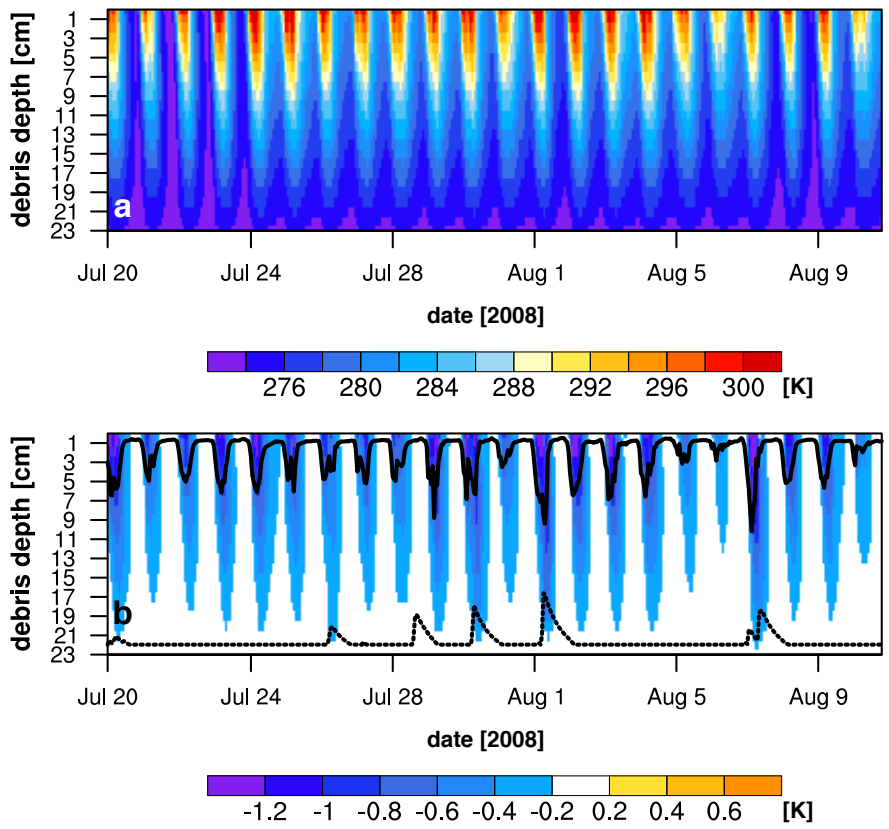

Fig. 9. Temporal and depth variation of **(a)** CMB-RES debris temperature and **(b)** the difference between the model runs (CMB-RES minus CMB-DRY). Units are K. For reference, QL (black solid curve) and debris water content (black dashed) are plotted without y-axes in panel **(b)**. The height of the debris-water curve shows the approximate level of moisture in the reservoir.

TCD
8, 1589–1629, 2014

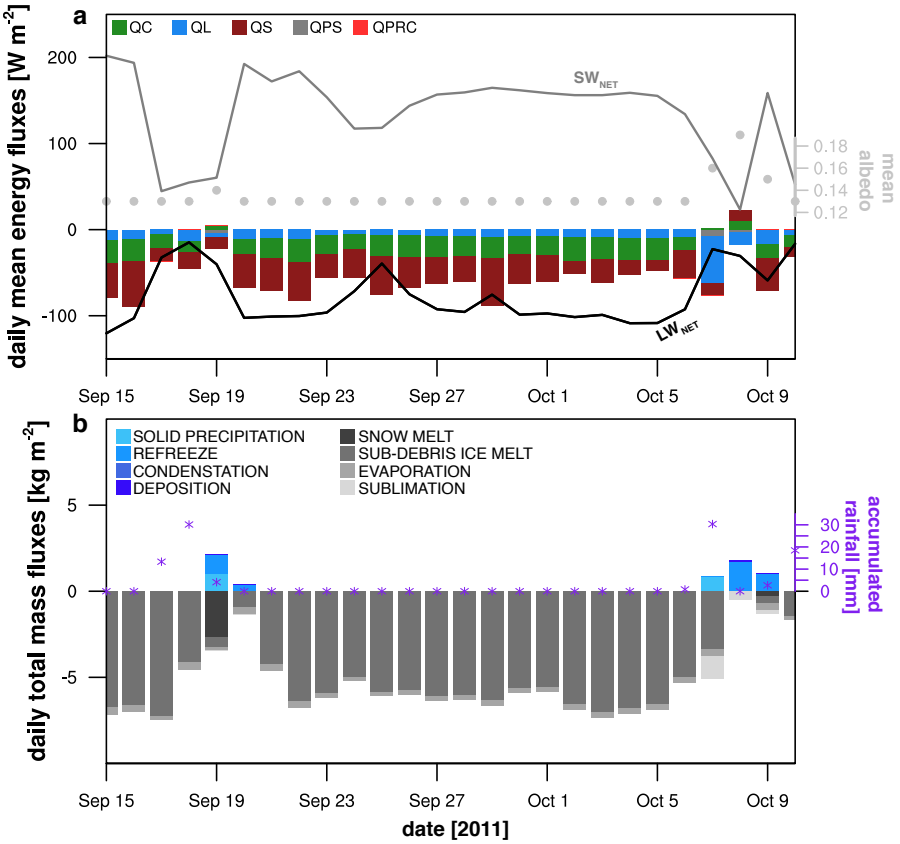

Fig. 10. Same as Fig. 6 but for the 2011 simulation.

TCD
8, 1589–1629, 2014

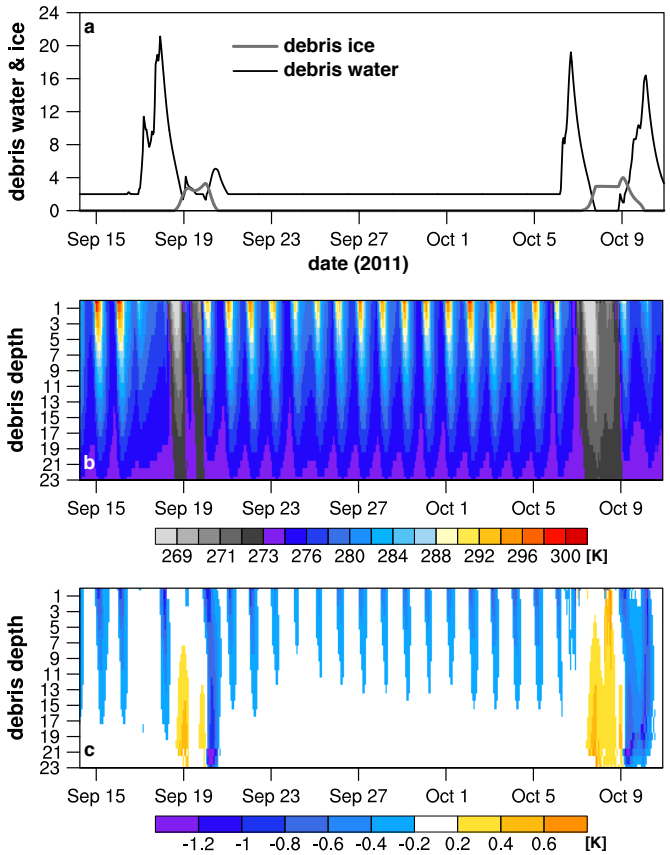

Fig. 11. (a) Time series from the 2011 simulation of the debris water (black line) and ice (grey line) content kg m^{-2}. Temporal and depth variation of **(b)** CMB-RES debris temperature and **(c)** the difference between the model runs (CMB-RES minus CMB-DRY). Units are K.

TCD
8, 1589–1629, 2014

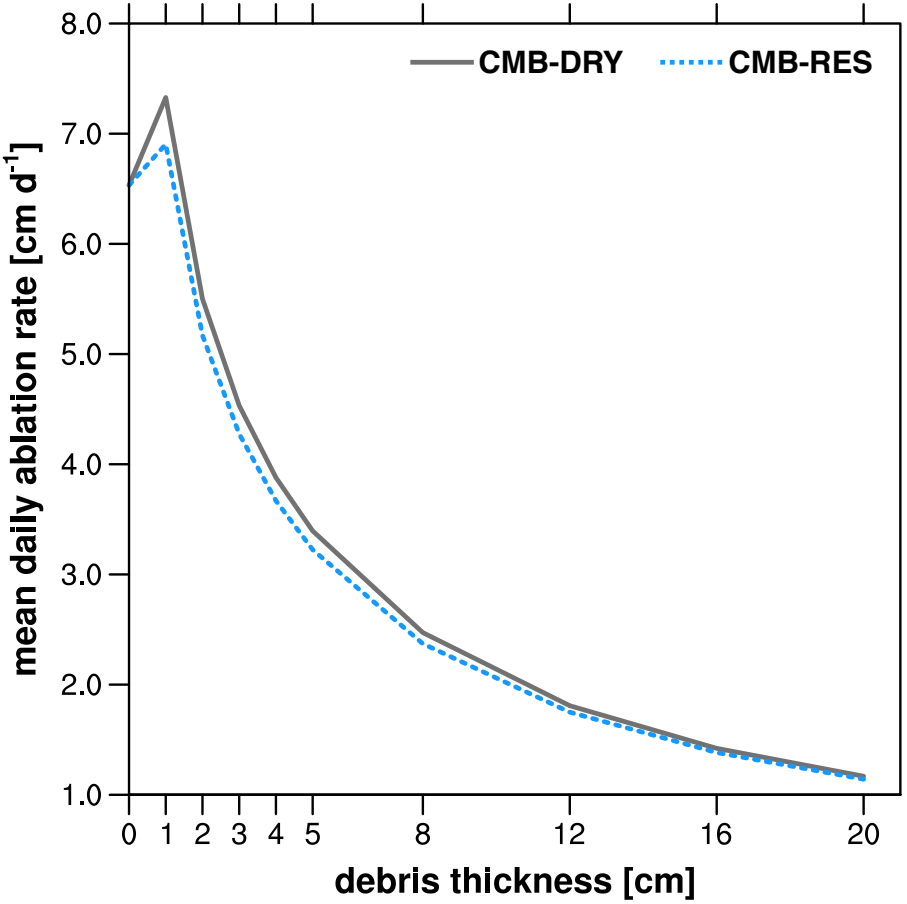

Fig. 12. Østrem curves, or daily mean ablation rate [cm d^{-1}] vs. debris thickness cm, produced by the CMB models using the forcing data from the 2008 simulation. CMB-DRY is the grey, solid curve and CMB-RES is the blue, dashed curve.

TCD
8, 1589–1629, 2014